ACSNANO

www.acsnano.org

ARTICLE

# Two-Dimensional-Material-Based Field-Effect Transistor Biosensor for Detecting COVID-19 Virus (SARS-CoV-2)

Parvin Fathi-Hafshejani, Nurul Azam, Lu Wang, Marcelo A. Kuroda, Michael C. Hamilton, Sahar Hasim,* and Masoud Mahjouri-Samani*

Cite This: *ACS Nano* 2021, 15, 11461−11469

Read Online

ACCESS | Metrics & More | Article Recommendations | Supporting Information

**ABSTRACT:** **The emergence of rapidly expanding infectious diseases such as coronavirus (COVID-19) demands effective biosensors that can promptly detect and recognize the pathogens. Field-effect transistors based on semiconducting two-dimensional (2D) materials (2D-FETs) have been identified as potential candidates for rapid and label-free sensing applications. This is because any perturbation of such atomically thin 2D channels can significantly impact their electronic transport properties. Here, we report the use of FET based on semiconducting transition metal dichalcogenide (TMDC) $WSe_2$ as a promising biosensor for the rapid and sensitive detection of SARS-CoV-2 *in vitro*. The sensor is created by functionalizing the $WSe_2$ monolayers with a monoclonal antibody against the SARS-CoV-2 spike protein and exhibits a detection limit of down to 25 fg/μL in 0.01X phosphate-buffered saline (PBS). Comprehensive theoretical and experimental studies, including density functional theory, atomic force microscopy, Raman and photoluminescence spectroscopies, and electronic transport properties, were performed to characterize and explain the device performance. The results demonstrate that TMDC-based 2D-FETs can potentially serve as sensitive and selective biosensors for the rapid detection of infectious diseases.**

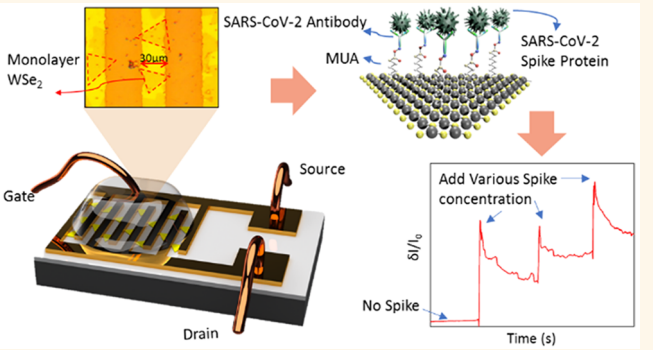


**KEYWORDS:** *SARS-CoV-2 spike protein, COVID-19, field-effect transistors, biosensors, 2D materials*

## INTRODUCTION

The world is continuously subject to the threat of highly contagious infectious diseases, some of which can be fatal or extremely detrimental to human health and societal interactions. For instance, in late 2019, coronavirus disease (COVID-19) produced by the severe acute respiratory syndrome coronavirus 2 (SARS-CoV-2) became a global public health threat. This virus quickly spread to most continents owing to the unavailability of appropriate therapy and diagnostics systems and was therefore categorized as a pandemic in March 2020.[1] Despite the tremendous progress in vaccine developments by a few pharmaceutical companies (e.g., Pfizer and Moderna), curbing the outbreak of the disease has been hampered by the production and distribution of drugs and vaccines as well as the emergence of new virus strains. Therefore, particular attention must still be given to developing diagnostic tools to quickly detect viruses such as SARS-CoV-2. Commonly, the real-time reverse transcription-polymerase chain reaction (RT-PCR) provides the only specific diagnostic test for the detection of COVID-19, based on the unique sequences of the virus RNA.[2] Several types of RT-PCR SARS-CoV-2 kits have been produced and approved, but the test is very time-consuming. Therefore, having alternative effective, rapid, and low-cost sensors for detecting viral antigens without sample preparation is crucial.[3−5]

Field-effect transistors (FET) have been attractive options for designing rapid, sensitive, and selective biosensors[6] that require a small number of test targets[7,8] for clinical diagnosis, on-site detection, and point-of-care testing.[9,10] For example, recently graphene-based FET biosensor has proven to be a rapid device for identifying SARS-CoV-2 spike protein with a

Received: February 7, 2021
Accepted: June 23, 2021
Published: June 28, 2021

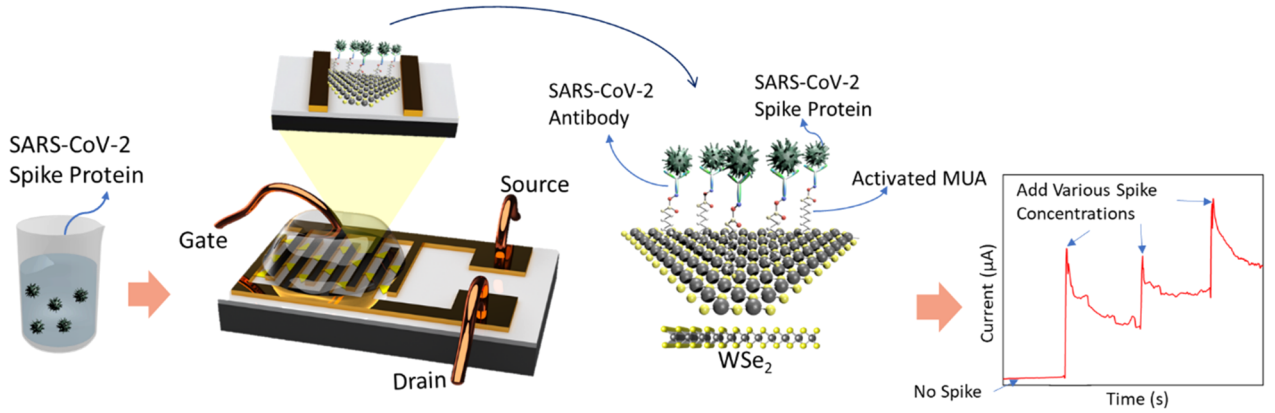


**Figure 1. Schematic diagram of the fabricated monolayer $WSe_2$-based FET COVID sensor. Monolayer $WSe_2$ crystals were used as the sensing material, interdigitated electrodes were fabricated on the crystals, SARS-CoV-2 antibody was immobilized onto the $WSe_2$ crystals via 11-mercaptoundecanoic acid (MUA), which was activated with n-hydroxysuccinimide (NHS) and carbodiimide hydrochloride (EDC) solution. The 2D-FET system could then sense the SARS-CoV-2 spike protein based on the corresponding effects on the electrical transport properties.**

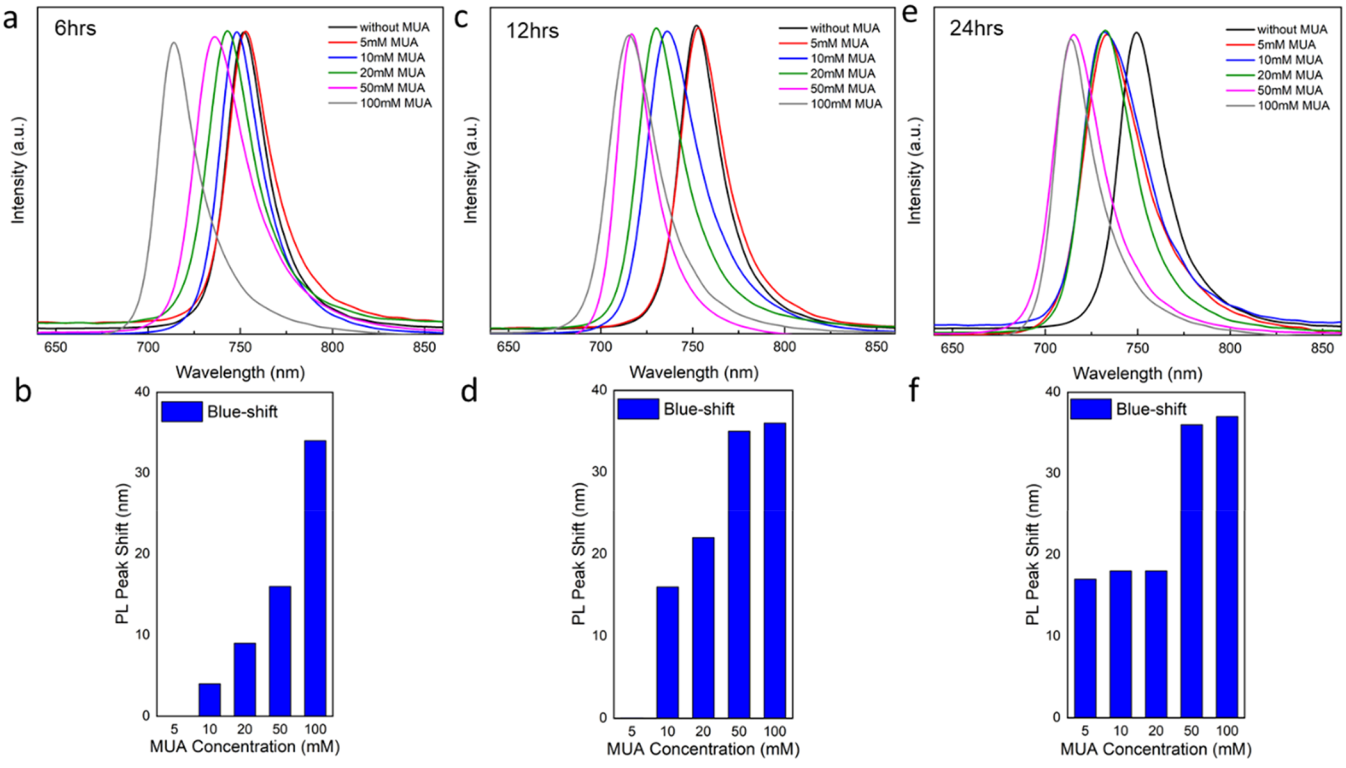


**Figure 2. PL spectra (a,c,e) and their corresponding emission wavelength shifts at each condition (b,d,f) of monolayer $WSe_2$ crystals functionalized by immersing into MUA/ethanol solution at room temperature. Columns correspond to the different time intervals of immersion (from top to bottom: 6, 12, 24 h). Spectrum colors denote the different concentrations (5, 10, 20, 50, and 100 mM). Higher MUA concentration and time resulted in a larger PL emission blue-shift.**

limit of detection (LOD) of 1 fg/mL.[11] Although graphene has high electron mobility, because of the graphene's near-zero bandgap, the off-state current leakage in graphene-based biosensors might increase, resulting in false signals.[12,13] Beyond graphene, semiconducting two-dimensional (2D) transition metal dichalcogenides (TMDCs) have recently emerged as promising materials for biosensing[14] among other applications[15−20] because of their promising optical, electrical, and mechanical properties.[21−26] TMDCs have exhibited relatively larger tunable bandgaps ranging from a few millielectron volts (meV) to a few electron volts (eV) depending on the 2D materials,[27,28] resulting in a reduced off-state current and better signal-to-noise ratios. Among the family of TMDCs, tungsten diselenide ($WSe_2$) with 1.67 eV bandgap[29,30] has shown the lowest detection limits and highest linear-regime sensitivities compared to, for example, molybdenum disulfide ($MoS_2$) for detecting streptavidin.[31] Moreover, monolayer $WSe_2$ crystals possess stronger absorption and higher surface activity than their multilayers, thereby enhancing the efficiency of the detection.[32] On account of these attractive properties as well as large surface areas and direct interaction with the molecules,


https://doi.org/10.1021/acsnano.1c01188
ACS Nano 2021, 15, 11461−11469

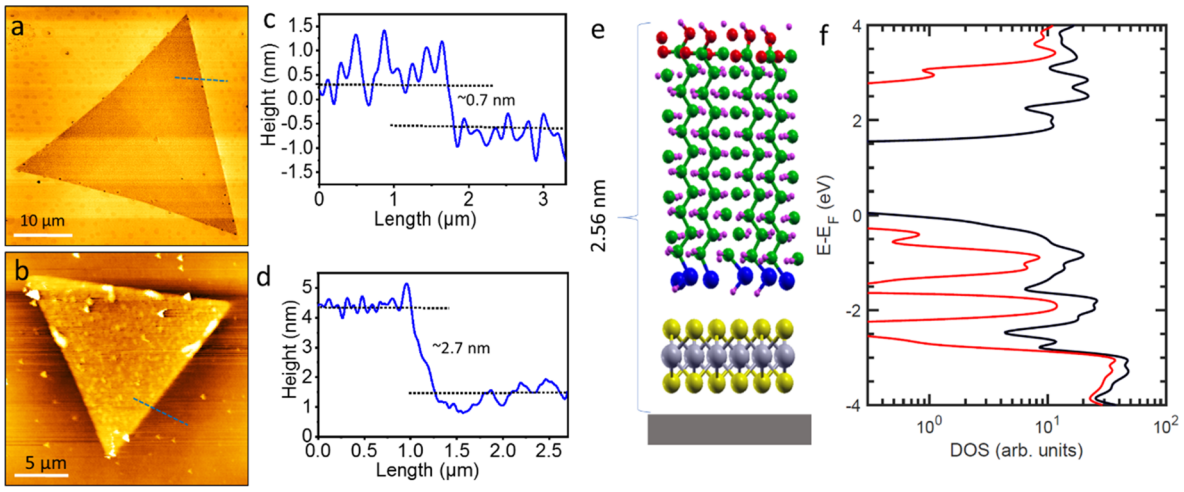


**Figure 3. AFM images and line profiles of the monolayer $WSe_2$ crystals prior to and after MUA functionalization. A pristine monolayer $WSe_2$ image (a) shows a clean and uniform topography with the line profile (c) of about ~0.7 nm corresponding to a single layer crystal. MUA-functionalized monolayer $WSe_2$ image (b) with a line profile of about 2.7 nm indicates full coverage of one vertically standing monolayer MUA on the $WSe_2$ crystal. (e) Schematic of MUA monolayer on top of $WSe_2$. (f) The density of states near the Fermi level of the full system (black) and the MUA (red) show that MUA states reside outside the band edge suggesting no charge transfer between the pristine TMDC and the molecule. Fermi level is placed ($E_F$) at the valence band edge of $WSe_2$.**

few-atom-thick TMDC crystals hold great potential in biosensing applications.[33−35]

In this study, we established the fabrication of 2D-FET biosensors using monolayer $WSe_2$ crystals for the detection of SARS-CoV-2 spikes proteins, as sketched in Figure 1. Monolayer $WSe_2$ crystals were functionalized with SARS-CoV-2 antibody as the base sensing platform employing 11-mercaptoundecanoic acid (MUA) as a probe linker. The FETs were fabricated by photolithographically defining interdigitated contact electrodes (i.e., source and drain) on the monolayer $WSe_2$ crystals combined with ionic liquid gating. We then tested the fabricated 2D-FET sensor for various SARS-CoV-2 spike protein concentrations down to 25 fg/$\mu$L. Experimental and theoretical studies, including density functional theory (DFT), Raman and photoluminescence (PL) spectroscopies, atomic force microscopy (AFM), and electronic transport properties were performed to monitor the optical and electrical response of the device at various stages of the fabrication and performance characterization to explain the observed phenomena.

## RESULTS AND DISCUSSION

**Concentration and Time Effect.** A critical step in developing the FET-based biosensors is to functionalize the surface of the active materials for improved biomatrix/channel interface. Recent studies have reported various self-assembled monolayers (SAMs) of organic disulfides, alkanethiols, and sulfides, which are strongly adsorbed on different metals and TMDCs.[36] To enhance the interaction between the biomolecules and the $WSe_2$ crystals in our 2D-FET biosensor, we functionalized the samples using a two-step process.[37] In the first step, the chemical linker 11-mercaptoundecanoic acid (MUA) was attached to the surface of the $WSe_2$ crystals. The SH terminated end of the MUA molecule strongly interacts with the chalcogen atoms and preferably vacancy sites on the surface of the $WSe_2$ crystal and attaches to its surface. The upper-end carboxyl group of the MUA molecule is then activated to form n-hydroxysuccinimide ester by exposure of MUA assembly to n-hydroxysuccinimide (NHS) and carbodiimide hydrochloride (EDC) solution at room temperature.[38,39] The active ester is susceptible to nucleophilic attack and will then react with amino groups provided by antibodies, leading to the formation of an amide bond.[37] This technique has also been reported by other groups[37,40] as an effective approach for connecting antibodies to various metals and TMDC materials.

To determine the optimum concentration and time needed for a successful conjugation, $WSe_2$ samples were immersed into various concentrations of MUA/ethanol (5, 10, 20, 50, and 100 mM) at different reaction times (6, 12, 24, and 30 h) at room temperature on an orbital shaker. We also evaluated several NHS/EDC ratios and reaction times to find the optimum activation conditions. Since the optical and electrical properties of such atomically thin 2D materials can be significantly altered depending on the surrounding medium and surface adsorbents, we monitored and analyzed the changes in the PL and Raman spectra of the samples at each step of the process.

Before the surface modifications, the peak wavelength of PL spectra of the as-synthesized $WSe_2$ crystals were at ~750 nm, as shown in Figure 2a,c,e (black lines). This is the typical emission wavelength of the $WSe_2$ crystals as also reported by others.[41−43] After functionalization of the $WSe_2$ surface with MUA molecules, we observed a clear blue-shift trend toward ~715 nm in the PL emission wavelength as a function of MUA concentration and interaction time. In general, higher MUA concentrations and longer interaction times resulted in a larger blue-shift until saturated at ~715 nm, as labeled in Figure 2a,c,e. The amount of PL shifts as a function of MUA concentration for each time interval is plotted in Figure 2b,d,f.

The self-assembled monolayers (SAM) of MUAs on $WSe_2$ crystals may occur by a combination of processes, which include chemisorption and physisorption. First, the chemisorption takes place when the $S^-$ of the MUA bonds to the Se vacancies in the $WSe_2$ crystals over time until all the vacancies are filled.[44] Simultaneously, this process heals defect states that may contribute to the elimination of midgap states. The rest of the surface is then uniformly coated with MUA molecules that


https://doi.org/10.1021/acsnano.1c01188
ACS Nano 2021, 15, 11461−11469

are physisorbed via van der Waals (vdW) interactions with other molecules and the TMDC surface. The possible causes of the blue-shift are[45] the enhanced dielectric environment upon coating,[46] the sulfur filling of the Se vacancies and formation of a quasi $WSe_{2-x}S_x$ structure on the surface,[47] and the removal of the defect levels. The Raman spectra of samples prepared at different conditions showed similar fingerprints with no significant variations (see Supporting Information), indicating the maintained integrity of the crystals during the process.

The AFM experiments were performed on $WSe_2$ samples before and after the MUA coating process. As presented in Figure 3a,c, the as-synthesized $WSe_2$ crystal showed a very clean surface with a height profile of ∼0.7 nm, expected for monolayer crystals.[48,49] For the AFM of the MUA coated sample, we chose to measure a coating condition that resulted in the maximum PL blue-shift (e.g., 100 mM for 24 h). As shown in Figure 3b,d, a uniform coating of the MUA on the entire crystal with a height profile of 2.8 nm ± 0.3 nm was observed (see Supporting Information). We modeled the MUA monolayer on top of the pristine $WSe_2$ monolayer using first-principles within the density functional theory (DFT), as presented in Figure 3e. Consistent with the AFM experiments and previous reports on the MUA length (∼1.7 nm),[50,51] this model yielded a height of 2.56 nm after accounting for the physical distance (2.25 nm) and vdW radii of H and Se (0.31 nm). We note that for the high-density limit of MUA molecules, interactions with adjacent molecules favor the vertical orientation that result in the MUA SAM. In addition, as shown in Figure 3f, analysis of the density of states (DOS) near the Fermi level indicates that the orbitals of MUA molecules reside outside the gap of the TMDC and, hence, no charge transfer is expected between the two components.

To optimize the activation process, we also examined three different NHS/EDC volume ratios (15 mM/75 mM, 100 mM/400 mM, and 100 mM/750 mM) and two different reaction times (3 and 6 h). We noticed that different ratios and molarities of NHS and EDC (15 mM/75 mM, 100 mM/400 mM, and 100 mM/750 mM) at different time intervals (3 and 6 h) did not show a significant difference in the PL data. Therefore, we choose the middle parameters of NHS, 100 mM, and EDC, 400 mM, at 6 h as a final concentration which was also used by others.[52]

After the activation process, we immersed the samples into a SARS-CoV-2 antibody solution, followed by the introduction of the SARS-CoV-2 spike protein (details are provided in the following sections) with different concentrations. Measurements of their optical characteristics revealed that the antibody and spike addition slightly red-shifted (∼5−10 nm) the PL emission wavelength. Figure 4 shows a large blue-shift in the normalized PL spectra of the samples after immersion in the MUA/ethanol solution and minor subsequent red-shifts after antibody and spike additions. This could find its origins charge transfer/doping process from the antibody and spike to the $WSe_2$ monolayer but confirmation would require a more comprehensive study.

**Fabrication and Characterization of 2D-FET Biosensor.** The 2D-FET biosensor in this experiment was designed based on interdigitated contact electrodes placed on the $WSe_2$ crystals to increase the detection area, as depicted in Figure 1. The optical image of an interdigitated 2D-FET sensor fabricated in this work is shown in Figure 5a. In general, the size of the synthesized $WSe_2$ crystals was in the range of 20−40 μm, and triangular crystals were randomly dispersed on the surface. The interdigitated source and drain electrodes were photolithographically patterned onto regions of the 2 × 1 $cm^2$ $Si/SiO_2$ substrates where the most $WSe_2$ crystals were located. Therefore, the effective sensing areas were different for each sample based on the number of $WSe_2$ monolayers connected between the interdigitated source and drain contacts.

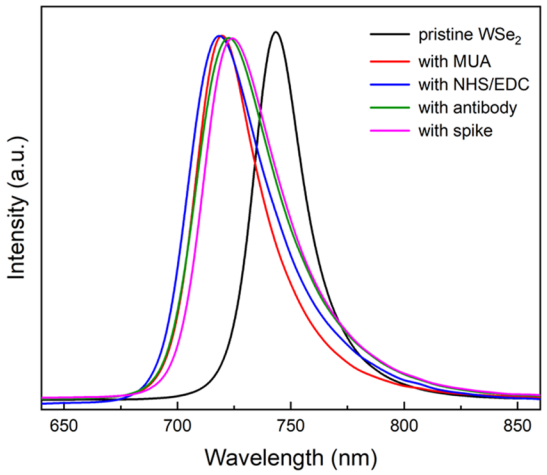


**Figure 4. Normalized PL spectra of the pristine $WSe_2$ (black curve) and after MUA attachment (red curve), NHS/EDC (blue curve), antibody attachment (green curve), and spike addition (pink curve).**

Electrical transport characteristics in the fabricated devices were monitored as a function of SARS-CoV-2 spike protein concentration. In this step, we first measured the electrical properties of devices with pristine $WSe_2$ monolayers prior to the addition of test solutions and molecules. The devices were gated using ionic liquid (0.01X PBS in deionized water) that enabled the addition of the SARS-CoV-2 spike protein directly into this solution for the exposure and detection process. Figure 5b shows the $I_{DS}-V_{DS}$ curves of the 2D-FET for the gate-to-source voltage ($V_{GS}$) ranging from −1 to 0 V in steps of 0.1 V. As $V_{GS}$ negatively increased, $I_{DS}$ amplitude increased, corresponding to an expected p-type semiconductor behavior of $WSe_2$ crystals.[53−55] Positive $V_{GS}$ values were not used since they caused the device to turn off. From this experiment, we choose a gate voltage of −0.5 V for subsequent measurements since it effectively turned on the device and was below the breakdown voltage of the PBS/water ionic solution for the tested configuration.

After measuring the electrical properties of the pristine $WSe_2$ sample, the crystals were functionalized by MUA and the $I_{DS}-V_{DS}$ behavior was remeasured. Finally, the SARS-CoV-2 antibody and spikes were added, and the $I_{DS}-V_{DS}$ behavior was measured again. Figure 5c shows the $I_{Ds}-V_{DS}$ curves of the device before and after the MUA functionalization of the $WSe_2$ channel and after the attachment of the antibody and spike protein. We also measured the $I_{DS}-V_{GS}$ transfer curves of the $WSe_2$-based FET after each modification process, as shown in Figure 5d. Following the MUA functionalization, the amplitude and slope of the $I_{DS}$ curve significantly decreased, suggesting a reduction of the number of mobile charges in the device channel. After the addition of the SARS-CoV-2 antibody and spikes, the device's current amplitude and its slope slightly increased again.


https://doi.org/10.1021/acsnano.1c01188
ACS Nano 2021, 15, 11461−11469

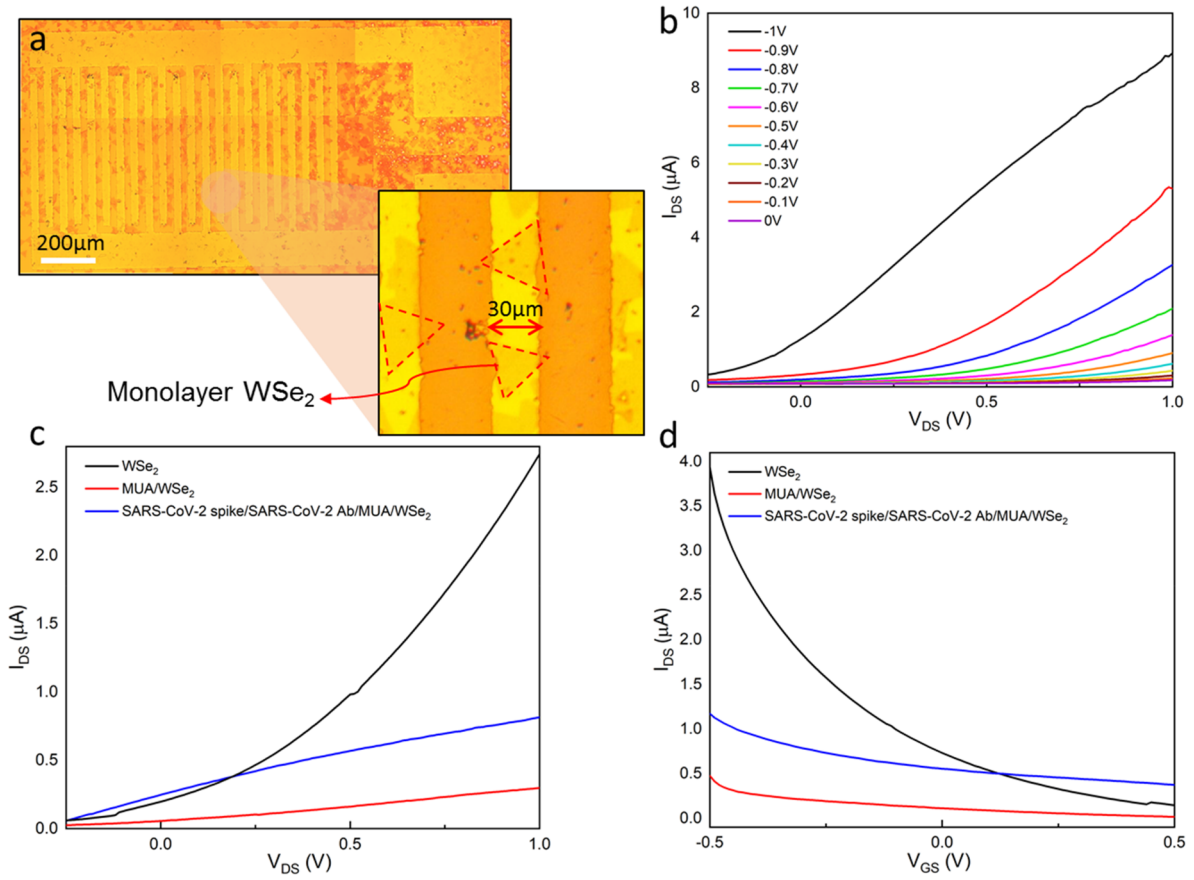


**Figure 5. Electrical characterization of pristine $WSe_2$, MUA-modified, and SARS-CoV-2 antibody and spike protein immobilized on $WSe_2$ crystals. Optical images of the $WSe_2$ COVID-19 2D-FET sensor (stitched images) and a close-up view showing the triangular 2D $WSe_2$ crystals in between the interdigitated electrodes (a). $I_{DS}$−$V_{DS}$ curves of a pristine $WSe_2$ FET with various gating voltages ($V_{GS}$) from −1 to 0 V in 0.1 V steps (b). $I_{DS}$−$V_{DS}$ curves (c) of the $WSe_2$-based device at each functionalization process, including pristine (black curve), with MUA (red curve), and with antibody and spike (blue curve). Corresponding $I_{DS}$−$V_{GS}$ curves (d) of the sensor with $V_{DS}$ = 1 V.**

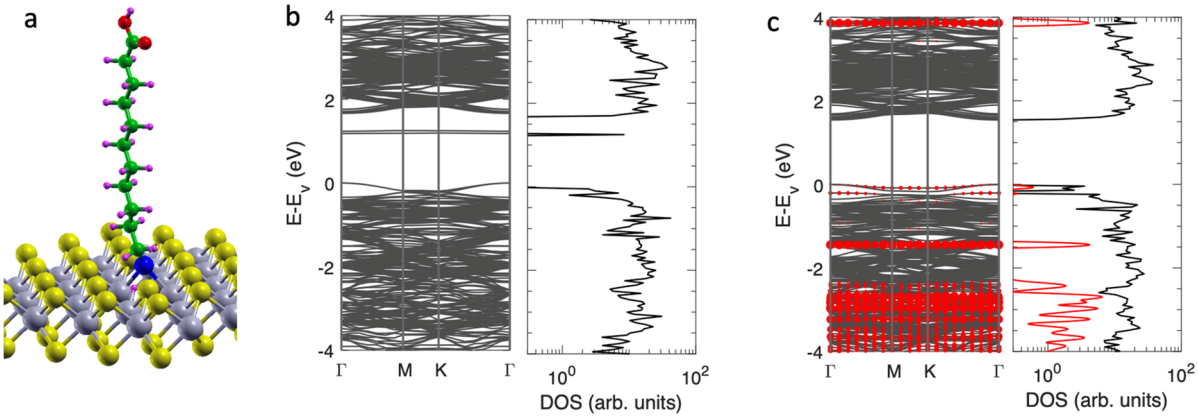


**Figure 6. Schematic of MUA adsorbed on a selenium vacancy site ($V_{Se}$) in the $WSe_2$ monolayer (a). Band structure and corresponding DOS of $WSe_2$ crystal with single $V_{Se}$ (b) and with adsorbed MUA molecule (c). To facilitate comparison, energies are referred to the valence band edge ($E_V$). The red symbols in (c) denote the contributions from localized atomic orbitals in the MUA molecule. The defect level located at ∼1.3 eV above the valence band edge is removed upon functionalization.**

Our DFT calculations shed light on a possible mechanism leading to decreased conductivity upon MUA functionalization. Namely, the Se vacancies that result in p-type behavior of $WSe_2$[54,56] may serve as a docking site for MUA molecules (Figure 6a). In this scenario, the Se vacancy ($V_{Se}$) and nearby dangling bonds become compensated by the S atom and H atom from MUA and remove the midgap states, as shown in Figure 6b,c. As a result of the MUA chemisorption, the *p*-type behavior of the device due to the vacancy filling becomes weaker.[31] The slight increase after the addition of the SARS-CoV-2 antibody and spikes is possibly due to charge transfer processes.

**Real-Time Detection of SARS-CoV-2 Antigen Spike Protein.** After understanding the transport characteristics at



https://doi.org/10.1021/acsnano.1c01188
ACS Nano 2021, 15, 11461−11469

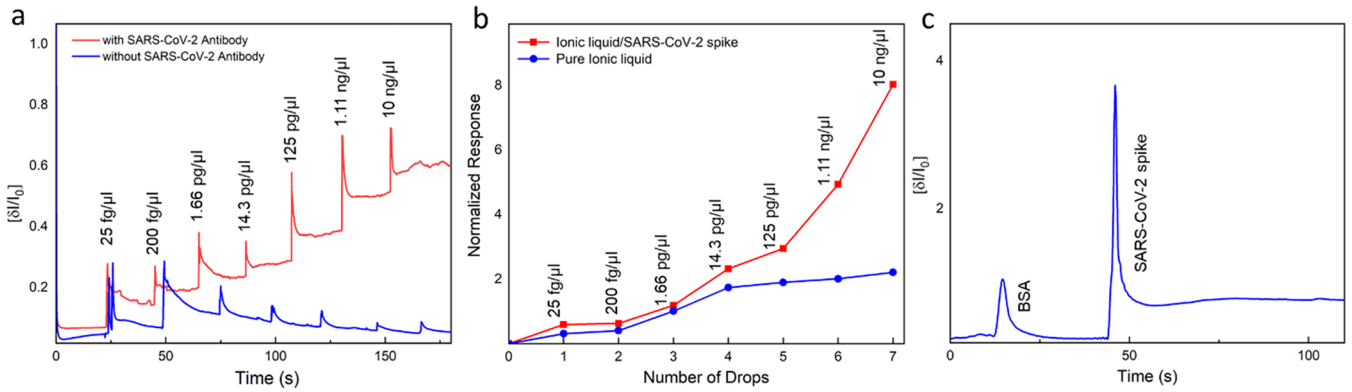


**Figure 7. Real-time detection of SARS-CoV-2 antigen spike protein. (a) Real-time response of $WSe_2$ COVID-19 2D-FET for various SARS-CoV-2 antigen spike protein with (red curve) and without antibody (blue curve) using $V_{DS}$ = 1 V, $V_{GS}$ = −0.5 V. (b) Comparing corresponding response plot for ionic liquid (0.01X PBS) with and without SARS-CoV-2 spike protein. (c) Selective response of COVID-19 FET sensor toward target BSA and SARS-CoV-2 antigen protein.**

various stages of the process, we investigated the real-time response of the devices with different concentrations of spike protein (Figure 7) to evaluate our COVID-19 2D-FET sensor performance. First, spike protein with different concentrations was prepared, and the final concentrations on the device were calculated after adding each drop for measurement (e.g., 25 fg/μL, 200 fg/μL, 1.66 pg/μL, 14.3 pg/μL, 125 pg/μL, 1.11 ng/μL, and 10 ng/μL) (see Supporting Information). The device's real-time output as a function of spike concentration was then measured by dropping 8 μL of the solution onto the device, as shown in Figure 7a,b. Clear stepwise changes were observed (red line in Figure 7a) for the device functionalized with the SARS-CoV-2 antibody, indicating an effective interaction of SARS-CoV-2 spikes protein with the antibodies. The device without the antibody showed only a slight change after introducing various spike concentrations (blue line in Figure 7a) that was well-below the response of the device with the antibody. This evidence indicated that the SARS-CoV-2 antibody plays an important role in the efficient interaction and detection of the SARS-CoV-2 spike protein. To ensure that the response of the device is due to the spike detection and not the ionic volume increase, we tested the device by adding a sequence of ionic 0.01X PBS drops (8 μL each) with and without the spike protein, as shown in Figure 7b. The device response to each spike protein concentration is normalized with respect to its response to the first ionic drop without the spike protein. Although for low spike concentrations, the difference in the signals was minimal, as the concentration increased a stark contrast in the device response emerged, evincing the potential of these $WSe_2$-based FET devices as biosensors. In addition, we tested the selectivity of the biosensor with 10 ng/μL bovine serum albumin (BSA) proteins and 10 ng/μL SARS-CoV-2 spike antigen protein on the same device. As shown in Figure 7c, the $WSe_2$-based COVID-19 FET sensor exhibited a negligible response to BSA proteins compared to its selective response to the SARS-CoV-2 spike antigen protein. Although this $WSe_2$-based FET biosensor has been successful in detecting the SARS-CoV-2 spike antigen proteins, it might also be a good platform for detecting other SARS-CoV-2 biomarkers such as cytokines.[57]

## CONCLUSION

In summary, we have introduced the potential application of 2D TMDC-based FETs as a promising biosensor for the rapid and sensitive detection of SARS-CoV-2 *in vitro*. The ability to easily functionalize the surface of these atomically thin monolayers with MUA allows for the production of selective biosensor devices targeting different infectious diseases. Using experimental and theoretical studies, we showed that the MUA molecules vertically self-assemble on the surface of the $WSe_2$ crystals. The MUA functionalized samples were further characterized by monitoring the optical and electrical properties. The adsorption of the MUA molecules onto the $WSe_2$ crystals resulted in a clear blue-shift in PL spectra from ∼740 to ∼720 nm. Results were rationalized using DFT calculations in terms of MUA chemisorption and physisorption processes on the surface of these TMDCs. The 2D FET sensors in this work were created by fabricating interdigitated electrodes on monolayer $WSe_2$ crystals followed by functionalizing the MUA on the $WSe_2$ monolayers with a monoclonal antibody against the SARS-CoV-2 spike protein. We demonstrated the detection down to 25 fg/μL in 0.01X PBS that may be further improved upon device optimization. Because of the current manufacturing challenges in fabricating uniform devices with consistent performance, the current magnitudes were different from device to device. The device's selectivity using BSA protein as the test molecule showed negligible response to BSA compared to the SARS-CoV-2 spike antigen protein. Theoretical and experimental studies, including DFT, AFM, Raman, and PL spectroscopies, and electronic transport properties, were performed to characterize and explain the device performance. This work demonstrated the potential application of emerging TMDC-based 2D-FETs as sensitive and selective biosensors for the rapid detection of infectious diseases.

## MATERIALS AND METHODS

**Fabrication of $WSe_2$–Based Sensing Devices.** Monolayer 2D $WSe_2$ crystals were synthesized using a laser-assisted synthesis technique developed in our lab.[58] Silicon samples with 250 nm of the thermal oxide layer were used as the substrates. The $WSe_2$ powders on the graphite boat (1.2 × 0.7 × 0.7 $cm^3$) were placed inside the 1 in. furnace tube. A continuous-wave $CO_2$ laser with a 10.6 μm wavelength was used to evaporate the $WSe_2$ powders and grow monolayer $WSe_2$ crystals on the $Si/SiO_2$ substrate placed on top of the graphite boat.

The devices with interdigitated electrodes on top of the $WSe_2$ crystals were fabricated employing conventional photolithography. Then, titanium electrodes were sputtered onto the patterns, followed


https://doi.org/10.1021/acsnano.1c01188
ACS Nano 2021, 15, 11461−11469

by a lift-off technique. The interdigitated device dimensions were about 2 × 1 $mm^2$ ($L \times W$). MUA, carbodiimide hydrochloride (EDC), and *N*-hydroxysuccinimide (NHS) were purchased from Sigma-Aldrich INC. SARS-CoV-2 spike protein and SARS-CoV-2 spike antibody were purchased from Sino Biological, Inc., U.S. (40150-R007). Bovine serum albumin (10 ng/μL) (BSA) was prepared in 0.01X PBS.

**Immobilization of SARS-CoV-2 Antibody on the $WSe_2$ Surface.** The fabricated $WSe_2$-based 2D-FET devices were immersed into pure ethanol with different concentrations 11-MUA for different intervals at room temperature on an orbital shaker. Devices were then taken out and rinsed with DI water and gently dried with nitrogen gas. The $WSe_2$ surface modified by 11-MUA were dipped into NHS and EDC with various ratios (15 mM/75 mM, 50 mM/200 mM, 100 mM/400 mM, and 100 mM/750 mM) and time (3 and 6 h) to activated MUA. The activated MUA surface was gently washed with ultrapure water and dried with nitrogen gas. Finally, the 3.3 ng/μL SARS-CoV-2 antibodies in 0.01X PBS (10 mM, pH 7.4) solution was added and incubated overnight. After overnight incubation, the surface was washed and ready for sensing of the target SARS-CoV-2 spike protein. SARS-CoV-2 spike protein with various concentrations (25 fg/μL, 200 fg/μL, 1.66 pg/μL, 14.3 pg/μL, 125 pg/μL, 1.11 ng/μL, and 10 ng/μL) in 0.01X PBS was applied to the biosensor surface by using a micropipette at the time of measurements.

**Optical and Morphological Measurements.** Pristine and MUA functionalized $WSe_2$ crystals were characterized by Raman spectroscopy, photoluminescence spectroscopy (PL), and atomic force microscopy (AFM). The measurements were performed in a confocal microconfiguration using a 50× microscope objective lens (NA = 0.75). We employed a Horiba HR spectrometer with a 1200 grooves/mm grating and a laser excitation wavelength of 532 nm. The AFM imaging was carried out using a HR-AFM Workshop system with 0.3 Hz scan rate and 512 resolution. The instrument was operated in the noncontact mode. The Gwyddion software was used for AFM data processing and analysis.

**Sensing Measurement.** The electrical performance was evaluated by a HP 4156A precision semiconductor analyzer and probe station. Also, Signatone probe tips model SE-BC (beryllium copper) were used for applying bias to the electrolyte. The detected electrical response signal was normalized as $[\Delta I/I_0] = (I - I_0)/I_0$, where $I$ is the detected real-time current and $I_0$ is the initial current.

**DFT Calculations.** Atomistic properties of the MUA-functionalized $WSe_2$ were calculated using first-principles calculations within the DFT. The supercells for the pristine monolayer $WSe_2$ crystal with and without MUA functionalization were created, and the atomic positions were fully relaxed until the forces become smaller than 0.005 eV/Å using Γ-point calculations. We employed the Perdew–Burke–Ernzerhof parametrization of the exchange-correlation functional and included the van der Waals dispersive forces,[59−62] as implemented in the quantum espresso software suite.[63] The core electrons are described by performing the projector augmented wave pseudopotentials[64] using energy cutoffs of 50 and 500 Ry for the wave function and density, respectively.

## ASSOCIATED CONTENT

### Supporting Information

The Supporting Information is available free of charge at https://pubs.acs.org/doi/10.1021/acsnano.1c01188.

Raman results of MUA functionalization, the real-time response of the sensor for pure 0.01X Pbs and SARS-CoV-2 antigen spike protein with and without $WSe_2$ crystals, extended time response of the sensor, optical images of the sensor with dropping process, AFM images, height profile measurements of MUA functionalized $WSe_2$ monolayers with surface roughness measurement data, and device-to-device response variations (PDF)

## AUTHOR INFORMATION


### Corresponding Authors

**Masoud Mahjouri-Samani** − *Department of Electrical and Computer Engineering, Auburn University, Auburn, Alabama 36849, United States;* orcid.org/0000-0002-6080-7450; Email: mahjouri@auburn.edu

**Sahar Hasim** − *Department of Biology, Mercer University, Macon, Georgia 31207, United States*; Email: sahar.hasim@mercer.edu

### Authors

**Parvin Fathi-Hafshejani** − *Department of Electrical and Computer Engineering, Auburn University, Auburn, Alabama 36849, United States*

**Nurul Azam** − *Department of Electrical and Computer Engineering, Auburn University, Auburn, Alabama 36849, United States;* orcid.org/0000-0002-9721-5141

**Lu Wang** − *Department of Physics, Auburn University, Auburn, Alabama 36849, United States*

**Marcelo A. Kuroda** − *Department of Physics, Auburn University, Auburn, Alabama 36849, United States;* orcid.org/0000-0002-7123-2138

**Michael C. Hamilton** − *Department of Electrical and Computer Engineering, Auburn University, Auburn, Alabama 36849, United States*

Complete contact information is available at: https://pubs.acs.org/10.1021/acsnano.1c01188


### Author Contributions

P.F. designed and performed the experimental setup, device fabrication, materials and device characterizations, data analysis, and manuscript writing. N.A. synthesized the 2D materials, performed AFM measurements, and participated in electrical characterizations and analysis. L.W. and M.A.K. performed theoretical DFT simulations and analyses. M.C.H. participated in electrical measurements and analysis. S.H. and M.M.S. led the project, participated in experimental design, data acquisition and analysis, discussions, and manuscript preparation. All of the authors participated in manuscript preparation and revision processes.

### Notes

The authors declare no competing financial interest.

## ACKNOWLEDGMENTS

This work is partially supported by the Auburn University Intermural Grant Program (IGP-VPR 180247). Alabama Micro/Nanoelectronic Science and Technology Center (AMNSTC) at Auburn University provided access to the cleanroom facility. Computational resources were provided by the AU Hopper and Easley HPC. The authors express great gratitude to S. Elafandi for his help with optical characterizations.

## REFERENCES

(1) World Health Organization, Coronavirus Disease 2019 (COVID-19): Situation Report − 52 (2020). https://www.who.int/docs/default-source/coronaviruse/situation-reports/20200312-sitrep-52-covid-19.pdf?sfvrsn=e2bfc9c0_4 (accessed on June 2020).

(2) Corman, V. M; Landt, O.; Kaiser, M.; Molenkamp, R.; Meijer, A.; Chu, D. K.; Bleicker, T.; Brunink, S.; Schneider, J.; Schmidt, M. L.; Mulders, D. G.; Haagmans, B. L; van der Veer, B.; van den Brink, S.; Wijsman, L.; Goderski, G.; Romette, J.-L.; Ellis, J.; Zambon, M.; Peiris, M.; Goossens, H.; Reusken, C.; Koopmans, M. P.; Drosten, C.

Detection of 2019 Novel Coronavirus (2019-nCoV) by Real-Time RT-PCR. *Eurosurveillance* **2020**, *25* (3), 2000045.
(3) Nelson, P. P.; Rath, B. A.; Fragkou, P. C.; Antalis, E.; Tsiodras, S.; Skevaki, C. Current and Future Point-of-Care Tests for Emerging and New Respiratory Viruses and Future Perspectives. *Front. Cell. Infect. Microbiol.* **2020**, *10*, 181.
(4) Layqah, L. A.; Eissa, S. An Electrochemical Immunosensor for the Corona Virus Associated with the Middle East Respiratory Syndrome Using an Array of Gold Nanoparticle-Modified Carbon Electrodes. *Microchim. Acta* **2019**, *186* (4), 224.
(5) Wu, K.; Klein, T.; Krishna, V. D.; Su, D.; Perez, A. M.; Wang, J.-P. Portable GMR Handheld Platform for the Detection of Influenza a Virus. *ACS sensors* **2017**, *2* (11), 1594−1601.
(6) Vu, C.-A.; Chen, W.-Y. Field-Effect Transistor Biosensors for Biomedical Applications: Recent Advances and Future Prospects. *Sensors* **2019**, *19* (19), 4214.
(7) Janissen, R.; Sahoo, P. K.; Santos, C. A.; da Silva, A. M.; von Zuben, A. A. G.; Souto, D. E. P.; Costa, A. D. T.; Celedon, P.; Zanchin, N. I. T.; Almeida, D. B.; Oliveira, D. S.; Kubota, L. T.; Cesar, C. L.; Souza, A. P. d.; Cotta, M. A.; et al. InP Nanowire Biosensor with Tailored Biofunctionalization: Ultrasensitive and Highly Selective Disease Biomarker Detection. *Nano Lett.* **2017**, *17* (10), 5938−5949.
(8) Liu, J.; Chen, X.; Wang, Q.; Xiao, M.; Zhong, D.; Sun, W.; Zhang, G.; Zhang, Z. Ultrasensitive Monolayer $MoS_2$ Field-Effect Transistor Based DNA Sensors for Screening of Down Syndrome. *Nano Lett.* **2019**, *19* (3), 1437−1444.
(9) Lei, Y.-M.; Xiao, M.-M.; Li, Y.-T.; Xu, L.; Zhang, H.; Zhang, Z.-Y.; Zhang, G.-J. Detection of Heart Failure-Related Biomarker in Whole Blood with Graphene Field Effect Transistor Biosensor. *Biosens. Bioelectron.* **2017**, *91*, 1−7.
(10) Zhou, L.; Mao, H.; Wu, C.; Tang, L.; Wu, Z.; Sun, H.; Zhang, H.; Zhou, H.; Jia, C.; Jin, Q.; Chen, X.; Zhao, J. Label-Free Graphene Biosensor Targeting Cancer Molecules Based on Non-Covalent Modification. *Biosens. Bioelectron.* **2017**, *87*, 701−707.
(11) Seo, G.; Lee, G.; Kim, M. J.; Baek, S.-H.; Choi, M.; Ku, K. B.; Lee, C.-S.; Jun, S.; Park, D.; Kim, H. G.; Kim, S.-J.; Lee, J.-O; Kim, B. T.; Park, E. C.; Kim, S. I. Rapid Detection of COVID-19 Causative Virus (SARS-CoV-2) in Human Nasopharyngeal Swab Specimens Using Field-Effect Transistor-Based Biosensor. *ACS Nano* **2020**, *14* (4), 5135−5142.
(12) Morales-Narváez, E.; Baptista-Pires, L.; Zamora-Gálvez, A.; Merkoçi, A. Graphene-Based Biosensors: Going Simple. *Adv. Mater.* **2017**, *29* (7), 1604905.
(13) Ménard-Moyon, C. c.; Bianco, A.; Kalantar-Zadeh, K. Two-Dimensional Material-Based Biosensors for Virus Detection. *ACS sensors* **2020**, *5* (12), 3739−3769.
(14) Huang, X.; Zeng, Z.; Bao, S.; Wang, M.; Qi, X.; Fan, Z.; Zhang, H. Solution-Phase Epitaxial Growth of Noble Metal Nanostructures on Dispersible Single-Layer Molybdenum Disulfide Nanosheets. *Nat. Commun.* **2013**, *4* (1), 1−8.
(15) Jariwala, D.; Sangwan, V. K.; Lauhon, L. J.; Marks, T. J.; Hersam, M. C. Emerging Device Applications for Semiconducting Two-Dimensional Transition Metal Dichalcogenides. *ACS Nano* **2014**, *8* (2), 1102−1120.
(16) Podzorov, V.; Gershenson, M.; Kloc, C.; Zeis, R.; Bucher, E. High-Mobility Field-Effect Transistors Based on Transition Metal Dichalcogenides. *Appl. Phys. Lett.* **2004**, *84* (17), 3301−3303.
(17) Joshi, N.; Hayasaka, T.; Liu, Y.; Liu, H.; Oliveira, O. N.; Lin, L. A Review on Chemiresistive Room Temperature Gas Sensors Based on Metal Oxide Nanostructures, Graphene and 2D Transition Metal Dichalcogenides. *Microchim. Acta* **2018**, *185* (4), 213.
(18) Elafandi, S.; Christiansen, R.; Azam, N.; Cichon, M.; Park, M.; Hamilton, M. C.; Mahjouri-Samani, M. Monolayer 2D Quantum Materials Subjected to Gamma Irradiation in High-Vacuum for Nuclear and Space Applications. *Appl. Phys. Lett.* **2020**, *116* (21), 213105.
(19) Mahjouri-Samani, M.; Lin, M.-W.; Wang, K.; Lupini, A. R.; Lee, J.; Basile, L.; Boulesbaa, A.; Rouleau, C. M.; Puretzky, A. A.; Ivanov, I. N.; Xiao, K.; Yoon, M.; Geohegan, D. B. Patterned Arrays of Lateral Heterojunctions within Monolayer Two-Dimensional Semiconductors. *Nat. Commun.* **2015**, *6* (1), 1−6.
(20) Yang, C.; Trikantzopoulos, E.; Nguyen, M. D.; Jacobs, C. B.; Wang, Y.; Mahjouri-Samani, M.; Ivanov, I. N.; Venton, B. J. Laser Treated Carbon Nanotube Yarn Microelectrodes for Rapid and Sensitive Detection of Dopamine *in Vivo*. *ACS sensors* **2016**, *1* (5), 508−515.
(21) Xia, F.; Wang, H.; Xiao, D.; Dubey, M.; Ramasubramaniam, A. Two-Dimensional Material Nanophotonics. *Nat. Photonics* **2014**, *8* (12), 899−907.
(22) Sarkar, D.; Xie, X.; Kang, J.; Zhang, H.; Liu, W.; Navarrete, J.; Moskovits, M.; Banerjee, K. Functionalization of Transition Metal Dichalcogenides with Metallic Nanoparticles: Implications for Doping and Gas-Sensing. *Nano Lett.* **2015**, *15* (5), 2852−2862.
(23) Wang, Q. H.; Kalantar-Zadeh, K.; Kis, A.; Coleman, J. N.; Strano, M. S. Electronics and Optoelectronics of Two-Dimensional Transition Metal Dichalcogenides. *Nat. Nanotechnol.* **2012**, *7* (11), 699−712.
(24) Ogawa, S. Magnetic Properties of 3D Transition-Metal Dichalcogenides with the Pyrite Structure. *J. Appl. Phys.* **1979**, *50* (B3), 2308−2311.
(25) Geohegan, D. B.; Puretzky, A. A.; Boulesbaa, A.; Duscher, G.; Eres, G.; Li, X.; Liang, L.; Mahjouri-Samani, M.; Rouleau, C.; Tennyson, W. Laser Synthesis, Processing, and Spectroscopy of Atomically-Thin Two Dimensional Materials. In *Advances in the Application of Lasers in Materials Science*; Ossi, P. M., Ed.; Springer, 2018; pp 1−37.
(26) Wang, K.; Huang, B.; Tian, M.; Ceballos, F.; Lin, M.-W.; Mahjouri-Samani, M.; Boulesbaa, A.; Puretzky, A. A.; Rouleau, C. M.; Yoon, M.; Zhao, H.; Xiao, K.; Duscher, G.; Geohegan, D. B. Interlayer Coupling in Twisted $WSe_2/WS_2$ Bilayer Heterostructures Revealed by Optical Spectroscopy. *ACS Nano* **2016**, *10* (7), 6612−6622.
(27) Bolotsky, A.; Butler, D.; Dong, C.; Gerace, K.; Glavin, N. R.; Muratore, C.; Robinson, J. A.; Ebrahimi, A. Two-Dimensional Materials in Biosensing and Healthcare: From *in Vitro* Diagnostics to Optogenetics and Beyond. *ACS Nano* **2019**, *13* (9), 9781−9810.
(28) Sarkar, D.; Liu, W.; Xie, X.; Anselmo, A. C.; Mitragotri, S.; Banerjee, K. $MoS_2$ Field-Effect Transistor for Next-Generation Label-Free Biosensors. *ACS Nano* **2014**, *8* (4), 3992−4003.
(29) Yun, W. S.; Han, S.; Hong, S. C.; Kim, I. G.; Lee, J. Thickness and Strain Effects on Electronic Structures of Transition Metal Dichalcogenides: 2H-$MX_2$ Semiconductors (M= Mo, W; X= S, Se, Te). *Phys. Rev. B: Condens. Matter Mater. Phys.* **2012**, *85* (3), 033305.
(30) Novoselov, K. S.; Geim, A. K.; Morozov, S. V.; Jiang, D.; Zhang, Y.; Dubonos, S. V.; Grigorieva, I. V.; Firsov, A. A. Electric Field Effect in Atomically Thin Carbon Films. *Science* **2004**, *306* (5696), 666−669.
(31) Nam, H.; Oh, B.-R.; Chen, M.; Wi, S.; Li, D.; Kurabayashi, K.; Liang, X. Fabrication and Comparison of $MoS_2$ and $WSe_2$ Field-Effect Transistor Biosensors. *Journal of Vacuum Science & Technology B, Nanotechnology and Microelectronics: Materials, Processing, Measurement, and Phenomena* **2015**, *33* (6), 06FG01.
(32) Lee, H. W.; Kang, D.-H.; Cho, J. H.; Lee, S.; Jun, D.-H.; Park, J.-H. Highly Sensitive and Reusable Membraneless Field-Effect Transistor (FET)-Type Tungsten Diselenide ($WSe_2$) Biosensors. *ACS Appl. Mater. Interfaces* **2018**, *10* (21), 17639−17645.
(33) Lv, R.; Robinson, J. A.; Schaak, R. E.; Sun, D.; Sun, Y.; Mallouk, T. E.; Terrones, M. Transition Metal Dichalcogenides and Beyond: Synthesis, Properties, and Applications of Single-and Few-Layer Nanosheets. *Acc. Chem. Res.* **2015**, *48* (1), 56−64.
(34) Kim, Y. H.; Kim, K. Y.; Choi, Y. R.; Shim, Y.-S.; Jeon, J.-M.; Lee, J.-H.; Kim, S. Y.; Han, S.; Jang, H. W. Ultrasensitive Reversible Oxygen Sensing by Using Liquid-Exfoliated $MoS_2$ Nanoparticles. *J. Mater. Chem. A* **2016**, *4* (16), 6070−6076.
(35) Agarwal, V.; Chatterjee, K. Recent Advances in the Field of Transition Metal Dichalcogenides for Biomedical Applications. *Nanoscale* **2018**, *10* (35), 16365−16397.


https://doi.org/10.1021/acsnano.1c01188
*ACS Nano* 2021, 15, 11461−11469

(36) Lee, W. H.; Park, Y. D. Tuning Electrical Properties of 2D Materials by Self-Assembled Monolayers. *Adv. Mater. Interfaces* **2018**, *5* (1), 1700316.
(37) Zhao, Q.; Duan, R.; Yuan, J.; Quan, Y.; Yang, H.; Xi, M. A Reusable Localized Surface Plasmon Resonance Biosensor for Quantitative Detection of Serum Squamous Cell Carcinoma Antigen in Cervical Cancer Patients Based on Silver Nanoparticles Array. *International Journal of Nanomedicine.* **2014**, *9*, 1097.
(38) Orelma, H.; Filpponen, I.; Johansson, L.-S.; Österberg, M.; Rojas, O. J.; Laine, J. Surface Functionalized Nanofibrillar Cellulose (NFC) Film as a Platform for Immunoassays and Diagnostics. *Biointerphases* **2012**, *7* (1), 61.
(39) Tsai, T.-C.; Liu, C.-W.; Wu, Y.-C.; Ondevilla, N. A. P.; Osawa, M.; Chang, H.-C. *In Situ* Study of EDC/NHS Immobilization on Gold Surface Based on Attenuated Total Reflection Surface-Enhanced Infrared Absorption Spectroscopy (ATR-SEIRAS). *Colloids Surf., B* **2019**, *175*, 300−305.
(40) Yuan, J.; Duan, R.; Yang, H.; Luo, X.; Xi, M. Detection of Serum Human Epididymis Secretory Protein 4 in Patients with Ovarian Cancer Using a Label-Free Biosensor Based on Localized Surface Plasmon Resonance. *Int. J. Nanomed.* **2012**, *7*, 2921.
(41) Tonndorf, P.; Schmidt, R.; Bottger, P.; Zhang, X.; Borner, J.; Liebig, A.; Albrecht, M.; Kloc, C.; Gordan, O.; Zahn, D. R. T.; Michaelis de Vasconcellos, S.; Bratschitsch, R. Photoluminescence Emission and Raman Response of Monolayer $MoS_2$, $MoSe_2$, and $WSe_2$. *Opt. Express* **2013**, *21* (4), 4908−4916.
(42) Huang, J.; Yang, L.; Liu, D.; Chen, J.; Fu, Q.; Xiong, Y.; Lin, F.; Xiang, B. Large-Area Synthesis of Monolayer $WSe_2$ on a $SiO_2$/Si Substrate and Its Device Applications. *Nanoscale* **2015**, *7* (9), 4193−4198.
(43) Brekhov, K.; Grishunin, K.; Ilyin, N.; Shestakova, A.; Lavrov, S.; Mishina, E. Optical Diagnostics of $WSe_2$ Monolayers. *Tech. Phys. Lett.* **2017**, *43* (12), 1112−1114.
(44) Kim, J.-S.; Yoo, H.-W.; Choi, H. O.; Jung, H. T. Tunable Volatile Organic Compounds Sensor by Using Thiolated Ligand Conjugation on $MoS_2$. *Nano Lett.* **2014**, *14* (10), 5941−5947.
(45) Jin, K.; Xie, L.; Tian, Y.; Liu, D. Au-modified Monolayer $MoS_2$ Sensor for DNA Detection. *J. Phys. Chem. C* **2016**, *120* (20), 11204−11209.
(46) Perebeinos, V.; Tersoff, J.; Avouris, P. Scaling of Excitons in Carbon Nanotubes. *Phys. Rev. Lett.* **2004**, *92* (25), 257402.
(47) Lin, Y.; Ling, X.; Yu, L.; Huang, S.; Hsu, A. L.; Lee, Y.-H.; Kong, J.; Dresselhaus, M. S.; Palacios, T. Dielectric Screening of Excitons and Trions in Single-Layer $MoS_2$. *Nano Lett.* **2014**, *14* (10), 5569−5576.
(48) Zhang, H.; Huang, J.; Wang, Y.; Liu, R.; Huai, X.; Jiang, J.; Anfuso, C. Atomic Force Microscopy for Two-Dimensional Materials: A Tutorial Review. *Opt. Commun.* **2018**, *406*, 3−17.
(49) Butler, S. Z.; Hollen, S. M.; Cao, L.; Cui, Y.; Gupta, J. A.; Gutierrez, H. R.; Heinz, T. F.; Hong, S. S.; Huang, J.; Ismach, A. F.; Johnston-Halperin, E.; Kuno, M.; Plashnitsa, V. V.; Robinson, R. D.; Ruoff, R. S.; Salahuddin, S.; Shan, J.; Shi, L.; Spencer, M. G.; Terrones, M.; Windl, W.; Goldberger, J. E. Progress, Challenges, and Opportunities in Two-Dimensional Materials Beyond Graphene. *ACS Nano* **2013**, *7* (4), 2898−2926.
(50) Tian, T.; Singhana, B.; Englade-Franklin, L. E.; Zhai, X.; Lee, T. R.; Garno, J. C. Surface Assembly and Nanofabrication of 1, 1, 1-Tris (Mercaptomethyl) Heptadecane on Au (111) Studied with Time-Lapse Atomic Force Microscopy. *Beilstein J. Nanotechnol.* **2014**, *5* (1), 26−35.
(51) Hinterwirth, H.; Kappel, S.; Waitz, T.; Prohaska, T.; Lindner, W.; Lämmerhofer, M. Quantifying Thiol Ligand Density of Self-Assembled Monolayers on Gold Nanoparticles by Inductively Coupled Plasma−Mass Spectrometry. *ACS Nano* **2013**, *7* (2), 1129−1136.
(52) Kamra, T.; Chaudhary, S.; Xu, C.; Montelius, L.; Schnadt, J.; Ye, L. Covalent Immobilization of Molecularly Imprinted Polymer Nanoparticles on a Gold Surface Using Carbodiimide Coupling for Chemical Sensing. *J. Colloid Interface Sci.* **2016**, *461*, 1−8.
(53) Choi, Y.; Kang, J.; Jariwala, D.; Kang, M. S.; Marks, T. J.; Hersam, M. C.; Cho, J. H. Low-Voltage Complementary Electronics from Ion-Gel-Gated Vertical van der Waals Heterostructures. *Adv. Mater.* **2016**, *28* (19), 3742−3748.
(54) Teng, F.; Hu, K.; Ouyang, W.; Fang, X. Photoelectric Detectors Based on Inorganic *p*-type Semiconductor Materials. *Adv. Mater.* **2018**, *30* (35), 1706262.
(55) Stanford, M. G.; Pudasaini, P. R.; Gallmeier, E. T.; Cross, N.; Liang, L.; Oyedele, A.; Duscher, G.; Mahjouri-Samani, M.; Wang, K.; Xiao, K.; Geohegan, D. B.; Belianinov, A.; Sumpter, B. G.; Rack, P. D. High Conduction Hopping Behavior Induced in Transition Metal Dichalcogenides by Percolating Defect Networks: Toward Atomically Thin Circuits. *Adv. Funct. Mater.* **2017**, *27* (36), 1702829.
(56) Liu, B.; Fathi, M.; Chen, L.; Abbas, A.; Ma, Y.; Zhou, C. Chemical Vapor Deposition Growth of Monolayer $WSe_2$ with Tunable Device Characteristics and Growth Mechanism Study. *ACS Nano* **2015**, *9* (6), 6119−6127.
(57) Kalantar-Zadeh, K.; Ward, S. A.; Kalantar-Zadeh, K.; El-Omar, E. M. Considering the Effects of Microbiome and Diet on SARS-CoV-2 Infection: Nanotechnology Roles. *ACS Nano* **2020**, *14* (5), 5179−5182.
(58) Azam, N.; Ahmadi, Z.; Yakupoglu, B.; Elafandi, S.; Tian, M.; Boulesbaa, A.; Mahjouri-Samani, M. Accelerated Synthesis of Atomically-Thin 2D Quantum Materials by a Novel Laser-Assisted Synthesis Technique. *2D Mater.* **2020**, *7* (1), 015014.
(59) Perdew, J. P.; Burke, K.; Ernzerhof, M. Generalized Gradient Approximation Made Simple. *Phys. Rev. Lett.* **1996**, *77* (18), 3865.
(60) Dion, M.; Rydberg, H.; Schröder, E.; Langreth, D. C.; Lundqvist, B. I. van der Waals Density Functional for General Geometries. *Phys. Rev. Lett.* **2004**, *92* (24), 246401.
(61) Thonhauser, T.; Cooper, V. R.; Li, S.; Puzder, A.; Hyldgaard, P.; Langreth, D. C. van der Waals Density Functional: Self-Consistent Potential and the Nature of the van der Waals Bond. *Phys. Rev. B: Condens. Matter Mater. Phys.* **2007**, *76* (12), 125112.
(62) Cooper, V. R. van der Waals Density Functional: An Appropriate Exchange Functional. *Phys. Rev. B: Condens. Matter Mater. Phys.* **2010**, *81* (16), 161104.
(63) Giannozzi, P.; Andreussi, O.; Brumme, T.; Bunau, O.; Nardelli, M. B.; Calandra, M.; Car, R.; Cavazzoni, C.; Ceresoli, D.; Cococcioni, M. Advanced Capabilities for Materials Modelling with Quantum ESPRESSO. *J. Phys.: Condens. Matter* **2017**, *29* (46), 465901.
(64) Blöchl, P. E. Projector Augmented-Wave Method. *Phys. Rev. B: Condens. Matter Mater. Phys.* **1994**, *50* (24), 17953.


https://doi.org/10.1021/acsnano.1c01188
*ACS Nano* 2021, 15, 11461−11469